Journal of Alloys and Compounds 1060 (2026) 187207

Contents lists available at ScienceDirect

Journal of Alloys and Compounds

journal homepage: www.elsevier.com/locate/jalcom

$SrAl_{12}O_{19}$:Mn phosphor prepared by the polymeric precursor method: A soft chemical route to reduce temperature synthesis for optical thermometry application

Thiago Ardana Chaim [a,*], Maria Inês Basso Bernardi [b], Adriano J.G. Otuka [a,c], Fabio Simões de Vicente [a], Alexandre Mesquita [a,c,**]

[a] São Paulo State University (UNESP), Institute of Geosciences and Exact Sciences, Multifunctional Materials & Applications, Rio Claro, SP, Brazil
[b] University of São Paulo - USP, São Carlos Institute of Physics, Nanomaterials and Advanced Ceramics, São Carlos, SP, Brazil
[c] São Paulo State University (UNESP), Institute of Geosciences and Exact Sciences, Research Center for Applied Natural Sciences – UNESPetro, Rio Claro, SP, Brazil

ARTICLE INFO

Keywords:
$SrAl_{12}O_{19}$
Mn^{4+}
$SrAl_{12}O_{19}$:Mn
Magnetoplumbite structure
Hexaluminate
Polymeric precursor method
Phosphor
Luminescence thermometry
Photoluminescence

ABSTRACT

Phosphor materials have attracted attention for their potential use in technological application such as optical thermometry, a non-contact temperature sensing technique which is based on the temperature-dependent luminescent properties of these materials. In many cases, these attractive properties are due to the incorporation of rare-earth elements into crystalline lattices, although their preparation is often toxic, costly and scarce. Thus, this study reports on the synthesis and characterization of manganese-doped strontium aluminate ($SrAl_{12}O_{19}:Mn^{4+}$), a rare-earth free phosphor for optical thermometry applications. As this magnetoplumbite host matrix typically requires high synthesis temperatures ($\geq$ 1300 °C) to stabilize, a soft chemical route based on the polymeric precursor method was implemented to reduce the preparation temperature. Combining annealing under N_2 atmosphere and applying very fast heating rate, crystallization temperature of the pure magnetoplumbite phase was successfully reduced by approximately 300 °C. The single-phase structure stabilizes at 1000 °C, a temperature notably lower than that required by solid-state reactions or conventional sol-gel methods. Structural characterization via X-ray diffraction (XRD) confirmed the formation of the hexagonal phase, whereas photoluminescence spectroscopy revealed the characteristic red emission of Mn^{4+} ions attributed to the $^2E \rightarrow {}^4A_2$ transition. Thus, Mn^{4+} ions effectively substituted Al^{3+} sites in the host lattice, resulting in strong red emission centered at 657 nm with high color purity. Temperature-dependent fluorescence measurements were performed and fluorescence intensity ratio (FIR) analysis indicated that the synthesized phosphors exhibit high thermal sensitivity ($S_{r\text{-}max}$ = 4.41%K^{-1}), comparable to rare-earth-doped materials and making the $SrAl_{12}O_{19}:Mn^{4+}$ phosphor a promising and cost-effective candidate for non-contact optical thermometry.

1. Introduction

Phosphors based on crystalline ceramic materials have been widely investigated due to their unique properties, such as optical performance, tunable emission, thermal, chemical and mechanical stabilities [1]. These properties enable a wide range of technological applications, including light-emitting diodes (LEDs), phosphor lamps, medical diagnostics and imaging (e.g., radiology, bio-imaging), electroluminescent devices, and emergency lighting systems [2–9]. Phosphor materials have also attracted attention for their potential application in optical thermometry, a non-contact temperature sensor technique which is based on the temperature-dependent luminescent properties of these materials, such as changes in emission intensity, bandwidth, polarization and lifetime [10–12]. This method has gained significant research interest due to its distinct advantages over traditional contact thermometers, including fast response times, miniaturization, and the ability to perform measurements remotely [10,12]. Furthermore, recent advancements have focused on developing strategies like dual-mode

* Corresponding author.
** Corresponding author at: São Paulo State University (UNESP), Institute of Geosciences and Exact Sciences, Multifunctional Materials & Applications, Rio Claro, SP, Brazil.
E-mail addresses: thiago.a.chaim@unesp.br (T.A. Chaim), alexandre.mesquita@unesp.br (A. Mesquita).

https://doi.org/10.1016/j.jallcom.2026.187207
Received 15 January 2026; Received in revised form 23 February 2026; Accepted 4 March 2026
Available online 6 March 2026

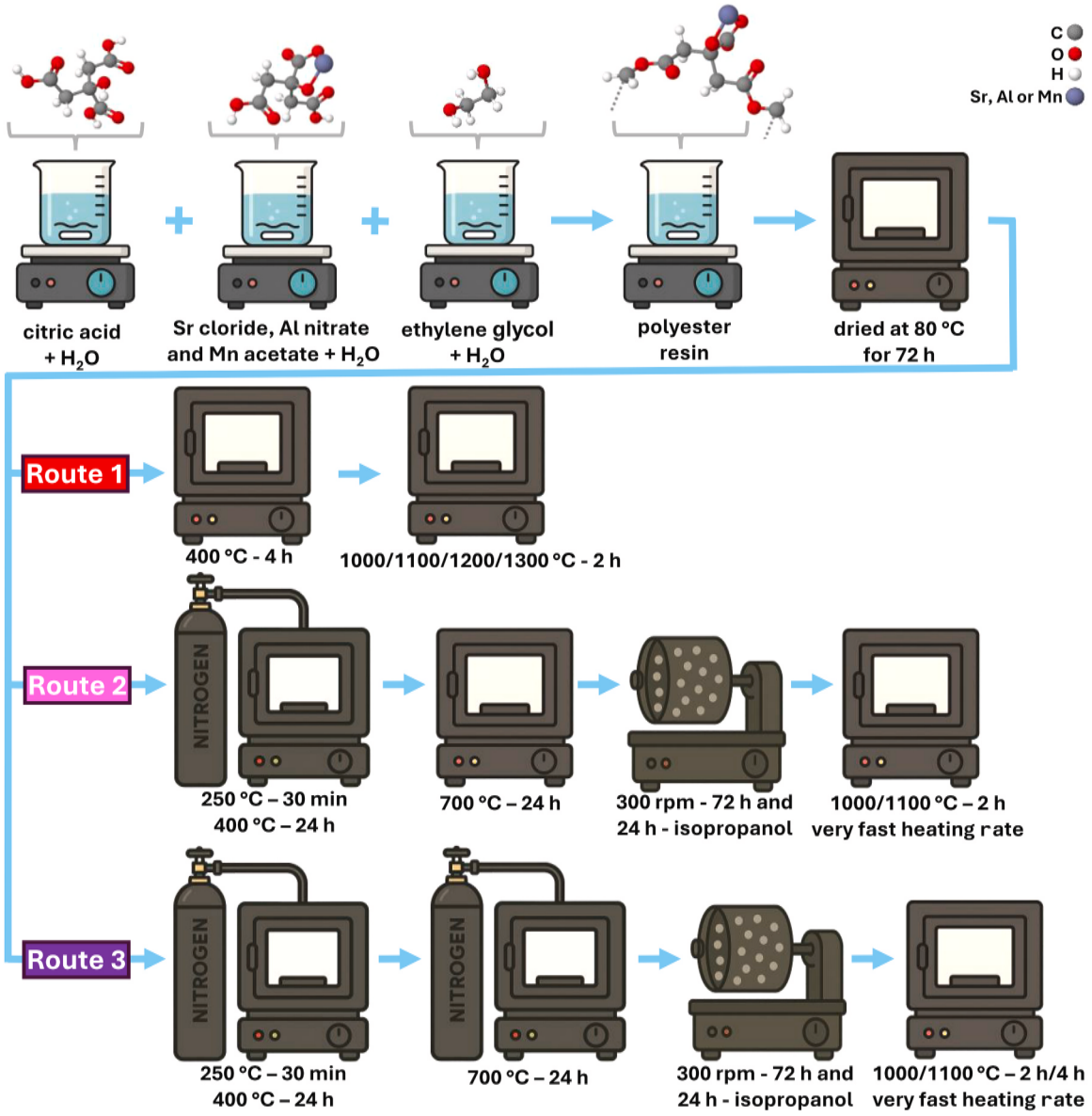

Fig. 1. Schematic illustration of the three experimental procedures to prepare SAM samples.

thermometry and utilizing materials with high thermal sensitivity, obtaining accurate and reliable sensing in wide temperature ranges [10,12].

In many cases, the attractive optical properties of phosphor materials are due to the incorporation of rare-earth elements on crystalline lattice as activator and/or sensitizer ions [4]. For example, several lanthanide-based materials are frequently applied in optical thermometry due to the fact that they are thermally stable, have relatively low phonon energies and narrow emission bands excited easily with low-cost diode lasers [12,13]. Moreover, because of the various band emissions observed in a single spectrum, these compounds can be suitable for use in the fluorescence intensity ratio (FIR) technique [10,12]. In the field of luminescence thermometry, FIR technique brings a significant advantage by using the intensities from two closely spaced energy levels whose changes with temperature are independent of the power source. Furthermore, any variation in excitation power affects both levels equally, enhancing the measurement sensitivity and sensor stability [12]. Nevertheless, it is worthy to emphasize that the preparation of rare-earth-based materials is often toxic, costly and scarce [4].

In this sense, manganese-doped strontium aluminate ($SrAl_{12}O_{19}Mn$) emerges as an interesting alternative to phosphor materials with strong red emission [14–16], such as $Y_2O_2S:Eu^{3+}$ and $Y_2O_3:Eu^{3+}$, which are inefficient and unstable [17], or nitrides and nitrogen oxides doped with Eu^{2+}, Tb^{3+} and Dy^{3+} ions, which show high quantum efficiency and thermal stability but economically not very interesting to prepare due to the critical reaction conditions, including the use of materials sensitive to conventional atmospheres and expensive rare-earth activators [14]. The red emission due to $^2E \rightarrow {}^4A_2$ transition of Mn^{4+} ions is also observed in Mn-doped arsenates and fluorides, but they contain toxic and harmful elements, which have long-term adverse effects on the environment [14,16]. Moreover, as a transition metal, Mn^{4+} ions have much higher absorption cross-section compared to rare-earth ions and their *f-f* transitions, enabling higher fluorescence brightness [10].

There are few reports at the literature about luminescence thermometry of Mn-doped $SrAl_{12}O_{19}$ compound [10,18,19]. Both of these papers report luminescence thermometry results through fluorescence intensity ratio (FIR) methodology, with values of maximum relative sensitivity ($S_{r,max}$) equal to 4.37 [19] and 0.27 [18] $\%K^{-1}$. The higher value was only achieved with FIR of Mn^{2+}/Mn^{4+} emissions, in which a strong Mn^{2+} emission was only obtained when these ions occupy

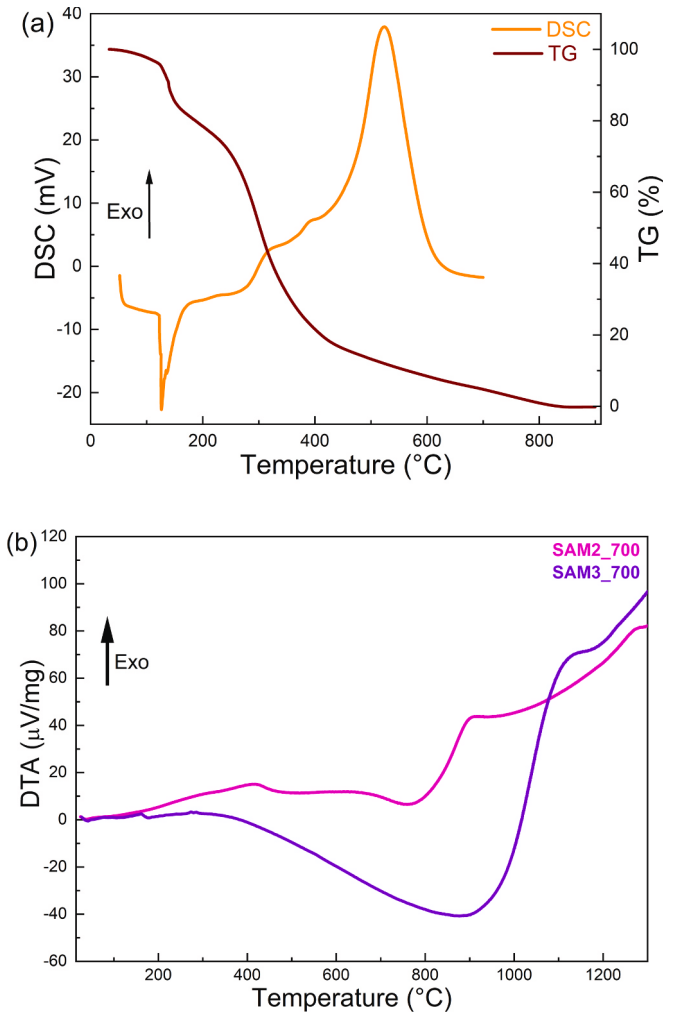

Fig. 2. (a) DSC and TG curves for dried resin and (b) DTA curves for SAM2_700 and SAM3_700 samples.

Ba-sites of a $BaAl_{12}O_{19}$-$SrAl_{12}O_{19}$ solid solution [19]. On the other hand, lower values of $S_{r,max}$ are observed for a single-phase host matrix of $SrAl_{12}O_{19}$ prepared by co-precipitation method with FIR calculated only for Mn^{4+} emission [18]. Thus, high values of $S_{r,max}$ for single-phase Mn-doped $SrAl_{12}O_{19}$ compound were not reported, making the preparation of this material with other synthesis routes an interesting issue to be explored in order to develop high thermal sensitivity for non-contact optical thermometry sensors.

The $SrAl_{12}O_{19}$:Mn (SAM) is a hexagonal aluminate compound whose structure is composed of layered alternating stacked spinel blocks of closed packed oxide ions and mirror planes with the general formula $AB_xAl_{12-x}O_{19}$, where A can be a large di- or trivalent cation in the mirror plane and B can be a transition-metal or noble metal ion, which can partially or completely substitute Al crystallographic sites [20]. This magnetoplumbite structure is stable even at temperatures up to 1600 °C, although requires high temperatures and time of annealing depending on the preparation method. The possibility of forming other strontium aluminates (variations in the Sr/Al ratio with a stoichiometric relationship of the type $Sr_xAl_{2y}O_{x+3y}$) and/or γ-Al_2O_3 in lower temperatures can be occur [20,21]. Several methodologies were used to synthesize $SrAl_{12}O_{19}$ samples always applying high temperatures in order to stabilize single phase of the magnetoplumbite structure: solid state reaction (1350 °C) [15], sol-gel (1200 °C) [22], polymeric precursor method (1200 °C) [23], co-precipitaion (1150 °C) [21]. Concerning polymeric precursor method, often called the modified Pechini method, this variation of sol-gel technique is commonly used to synthetize oxide

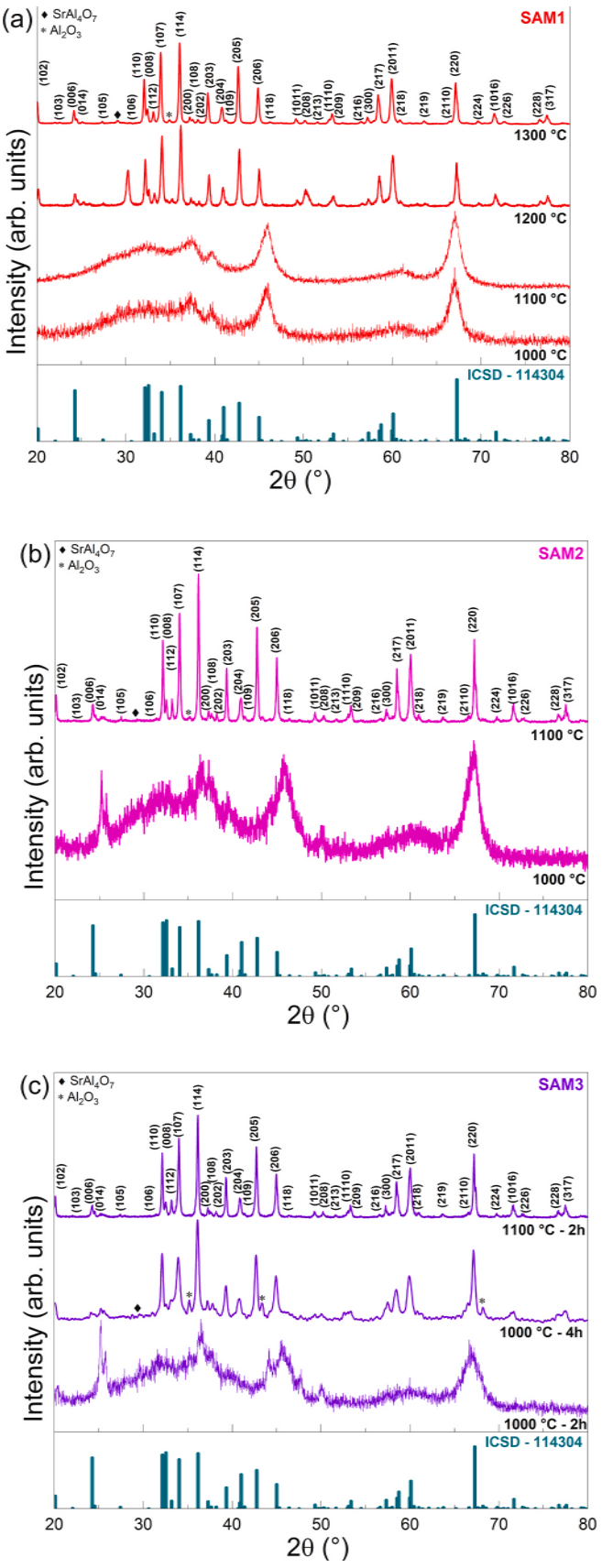

Fig. 3. XRD patterns for (a) SAM1, (b) SAM2 and (c) SAM3 samples.

Table 1
Comparison between synthesis methods to prepare $SrAl_{12}O_{19}$ compound.

Method	Synthesis temperature (°C)	Phases	Ref.
Solid state reaction	1600	$SrAl_{12}O_{19}$, $BaAl_{12}O_{19}$,	[19]
Solid state reaction	1200–1400	$SrAl_{12}O_{19}$, $SrAl_2O_4$, $SrAl_4O_7$	[25]
Solid state reaction	1350	$SrAl_{12}O_{19}$	[15]
Sol-gel	1200	$SrAl_{12}O_{19}$	[26]
Co-precipitation	1300	$SrAl_{12}O_{19}$, $SrAl_2O_4$, $SrAl_4O_7$	[18]
Co-precipitation	1200	$SrAl_{12}O_{19}$	[27]
Co-precipitation	1200	$SrAl_{12}O_{19}$	[28]
Co-precipitation	1150	$SrAl_{12}O_{19}$	[21]
Combustion	800	$SrAl_{12}O_{19}$, $SrAl_4O_7$	[29]
Polymeric precursor	1200	$SrAl_{12}O_{19}$	[23]
Polymeric precursor[a]	1300	$SrAl_{12}O_{19}$, $SrAl_4O_7$, Al_2O_3	this work
Polymeric precursor[b]	1100	$SrAl_{12}O_{19}$, $SrAl_4O_7$	this work
Polymeric precursor[c]	1100	$SrAl_{12}O_{19}$	this work
Polymeric precursor[d]	1000	$SrAl_{12}O_{19}$, $SrAl_4O_7$	this work

[a] SAM1_1300
[b] SAM2_1100
[c] SAM3_1100
[d] SAM3_1000 samples

Table 2
Semi-quantitative phase analysis obtained by XRD diffractograms for SAM samples.

Sample	Quantity of the phases (%)		
	$SrAl_{12}O_{19}$	Al_2O_3	$SrAl_4O_7$
SAM1_1300	93	4	3
SAM2_1100	97	2	1
SAM3_1100	100	0	0
SAM3_1000)	79	16	5

materials [24]. It works by first chelating metal cations with an α-hydroxycarboxylic acid (like citric acid) to form stable metal complexes. These complexes then polymerize with a polyhydroxy alcohol (such as ethylene glycol), resulting in a polymeric resin. This resin is then subjected to pyrolysis. This method offers several advantages, including its low toxicity, excellent compositional homogeneity, the ability to achieve doping at a molecular level in solution and a reduced tendency for metal ion segregation [24]. However, as well as solid state reaction, sol-gel, co-precipitation, hydrothermal, combustion, high temperatures are required to stabilize the magnetoplumbite structure [15,18,19,23,25–29]. To the best of our knowledge, only one paper available at the literature describes synthesis temperature of 1200 °C to prepare pure phase of $SrAl_{12}O_{19}$ through polymeric precursor method [23], without reports of Mn-doped samples. This methodology has also been applied to prepare yttrium aluminates combining a preliminary gradual pyrolytic decomposition under nitrogen flux to remove process of organic residues (avoiding the formation of molecular level inhomogeneities), chemically homogeneous ball-milled amorphous particles and very fast heating rates [30,31]. As a result, the synthesis temperature reduced several hundred Celsius degrees [30,31].

Thus, this study aimed to prepare $SrMn_{0.005}Al_{11.995}O_{19}$ (SAM) samples through the polymeric precursor method allied with annealing under N_2 atmosphere, ball-mill and very fast heating rate conditions. Consequently, reduction in synthesis temperature is expected as aforementioned. Therefore, the manuscript describes a variation in the preparation of polymeric precursor method in order to reduce the synthesis temperature and characterize optical properties of Mn-doped $SrAl_{12}O_{19}$ samples which can be applied in luminescence thermometry. Hence, SAM samples with this Mn composition were prepared since this concentration has been described as the optimized amount in terms of the fluorescence quenching [15]. The structure of SAM samples was characterized with X-ray diffraction (XRD) technique whereas field-emission scanning electron microscopy (SEM) probed their morphology. Thermal processes during the synthesis were analyzed via differential scan calorimetry (DSC), differential thermal (DTA) and termogravimetric (TG) analysis techniques. Fluorescence measurements were performed as a function of the temperature for non-contact optical thermometry applications.

2. Experimental procedure

The metallic precursor materials to synthesize SAM samples were strontium chloride hexahydrate ($Cl_2Sr{\cdot}6\ H_2O$, 99%, Sigma-Aldrich), aluminum nitrate ($Al(NO_3)_3{\cdot}9\ H_2O$, 98%, Vetec), manganese acetate ($C_4H_6MnO_4{\cdot}6\ H_2O$, ≥ 99%, Sigma-Aldrich). They were completely dissolved in deionized water at ambient temperature, followed by the addition of citric acid ($C_6H_8O_7$, 99.5%, Synth) under constant stirring until the total dissolution. The proportion of citric acid/metal was 3 mols of citric acid to 1 mol of metal. The polyesterification was achieved by adding ethylene glycol ($C_2H_6O_2$, 99.5%, Synth) under constant stirring with molar ratio of citric acid to ethylene glycol set at 3:2. A viscous polymeric resin with slight yellow coloration was obtained after the evaporation of water excess at a temperature of 90 °C for 4 h. Then, the resin was dried at 80 °C for 72 h.

After this procedure, three different routes were performed to prepare SAM samples. Route 1 involves the annealing of the dried resin at 400 °C for 4 h with a heating rate of 10 °C/min. Subsequently, the resultant powder was annealed at 1000, 1100, 1200 and 1300 °C for 4 h with a heating rate of 10 °C/min. Both steps occur in a conventional atmosphere. The samples under these experimental conditions were labeled as SAM1_X, where X is the annealing temperature of the latest thermal treatment in Celsius degrees. In the Route 2 procedure, the dried resin was thermally treated under N_2 flux at 250 °C using a heating rate of 1 °C/min during 30 min. This was an important step to avoid uncontrolled combustions inducing hot spots and the consequent formation of chemical inhomogeneities [30]. After this initial treatment, the material became a dried porous solid with dark brown coloration, which was annealed at 400 °C for 24 h under constant N_2 flux followed by another annealing at 700 °C for 24 h in conventional atmosphere, both of them with heating rate of 10 °C/min. The resultant material was ball-milled using yttria-stabilized zirconia spheres in two stages: dry ball-milled during 72 h in first step whereas isopropanol was added during 24 h in second one. This methodology in the milling promotes improvement in the homogeneity and reactivity of the amorphous powder. The dry medium during the milling causes effective crushing due to high attrition mechanisms whereas powder recovery is achieved in the wet medium stage [30]. Afterward, an annealing with very fast heating rate was performed at 1000 and 1100 °C for 2 h. This very fast rate consists in heating the furnace until reaching the equilibrium at a given temperature and then placing the sample inside. In this case and following the nomination for Route 1, samples were labeled as SAM2_1000 and SAM2_1100. Finally, the Route 3 is similar to Route 2, where the only differences are in the annealing at 700 °C, which is performed under constant N_2 flux, and an additional annealing at 1000 °C for 4 h. The Fig. 1 presents a schematic illustration of the experimental procedure of the three routes to prepare SAM samples. In Route 3, samples were labeled as SAM3_1000 and SAM3_1100.

Thermal analysis using TG, DTA and DSC techniques for SAM samples were performed with Shimadzu TG-50, DTA-50 and DSC-50 equipment, respectively. Room-temperature XRD analysis was made with measurements using a Rigaku Ultima 4 powder diffractometer. This

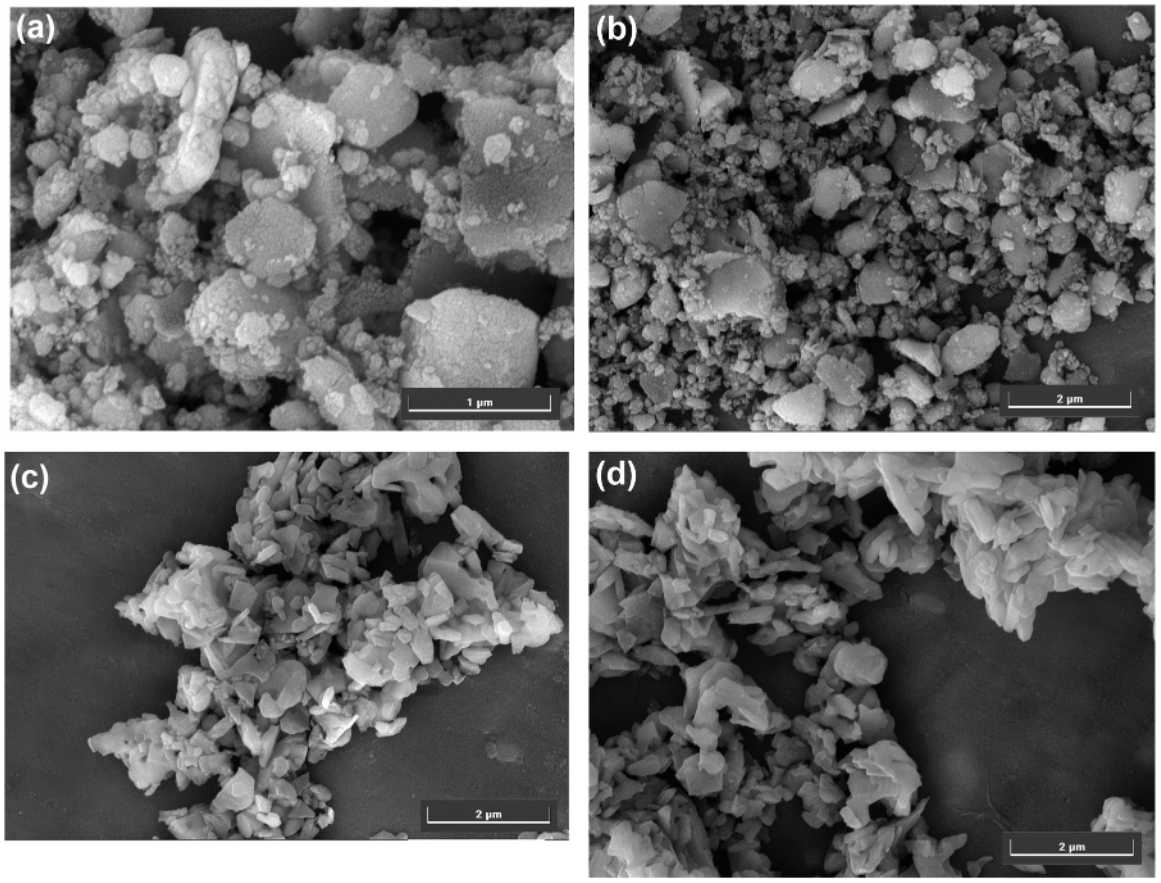

Fig. 4. SEM images for SAM1_1300 ((a) and (b)) and SAM3_1000 ((c) and (d)) samples with different magnifications.

instrument, configured in a θ−2θ geometry, was equipped with a rotating anode X-ray source emitting Cu-Kα radiation (λ = 1.542 Å) and a scintillation detector. Data were collected with 0.02° step size and a 5-second dwell time per step. SEM micrographs were achieved using a Tescan Mira (FEG) scanning electron microscope. Photoluminescence excitation and emission spectra at room temperature were measured at a Varian Cary Eclipse spectrophotometer. Temperature-dependent fluorescence spectra were collected using an Ocean Optics spectrophotometer integrated with a heating unit. Fluorescence measurements as function of the temperature were excited using a 405 nm laser operating at 0.5 W.

3. Results and discussion

In order to analyze thermal events during the synthesis, the dried resin (before the annealing with the three routes) was characterized with DSC and TG techniques under synthetic air, whereas DTA curves were collected for the powders after the annealing at 700 °C for Routes 2 and 3 under N_2 flux. The results are depicted in Fig. 2(a). As can be seen in this Fig for the dried resin, several thermal events are overlapped in DSC curve; all of them involve some kind of mass losses as TG curve at the same temperature intervals reveals. The first endothermic events are related to the dehydration of the resin (room temperature – 126 °C) and the elimination of physisorbed water (126 – 160 °C) with mass losses of about 4% and 11%, respectively [21]. Afterward this endothermic interval, several overlapped exothermic events attributed to the polymeric decomposition of the resin can be observed between 160 and 619 °C. At least, four exothermic events can be identified in this region: i) polymer degradation between 160 – 242 °C with mass loss of 9%, ii) polymeric degradation (-CH_2- groups) between 242 and 325 °C with mass loss of 35%, iii) polymeric degradation (-CO- groups) between 325 and 401 °C with mass loss of 22% and iv) polymeric degradation (-COO- groups) between 401 and 619 °C [32]. In the last event in TG curve, a mass loss is noticeable up to 840 °C, temperature much higher than the interval of the last DSC exothermic feature. This result infers that the remanent powder still loses weight due to residual carbon even after the completed polymeric degradation process. This finding agrees with previous studies which describe the synthesis of oxide compounds through the polymeric precursor method [33,34].

Fig. 2(b) exhibits DTA curves for the resultant powder after the annealing at 700 °C through Routes 2 and 3. For SAM2 sample, two broad exothermic peaks at around 420 and 657 °C can be observed, which can be ascribed to the decomposition of residual carbon as pointed out by DSC curve of the dried resin. Two other peaks positioned at around 895 and 1276 °C are also observed. The exothermic event at around 895 °C can be ascribed to the crystallization of γ-Al_2O_3, which has been reported to occur at the range of 876 – 920 °C, or the decomposition of $SrCO_3$ into SrO, whose temperature has been observed at around 900 °C [21,35]. Another exothermic event at around 1276 °C is attributed to solid state reaction of strontium aluminate from the precursor oxides. On the other hand, the DTA curve for SAM3 depicts different thermal behavior, showing a pronounced broadened endothermic event between ~ 378 and ~ 921 °C. This feature is related to the pyrolysis of the remanent organic material from the synthesis since all the thermal treatments of this sample were performed under N_2 flux, avoiding its elimination. Moreover, an exothermic peak is observed to be initialized at around 1115 °C and can be ascribed to crystallization of a strontium aluminate phase. Fig. S1 of the Supporting Information shows an optical micrography image of fractured section powder for SAM3 samples after the annealing at 700 °C under N_2 flux, depicting a whitish powder within a blackened shell. This Fig. also exhibits Raman spectra for the white and black parts of the material, revealing that the remanent

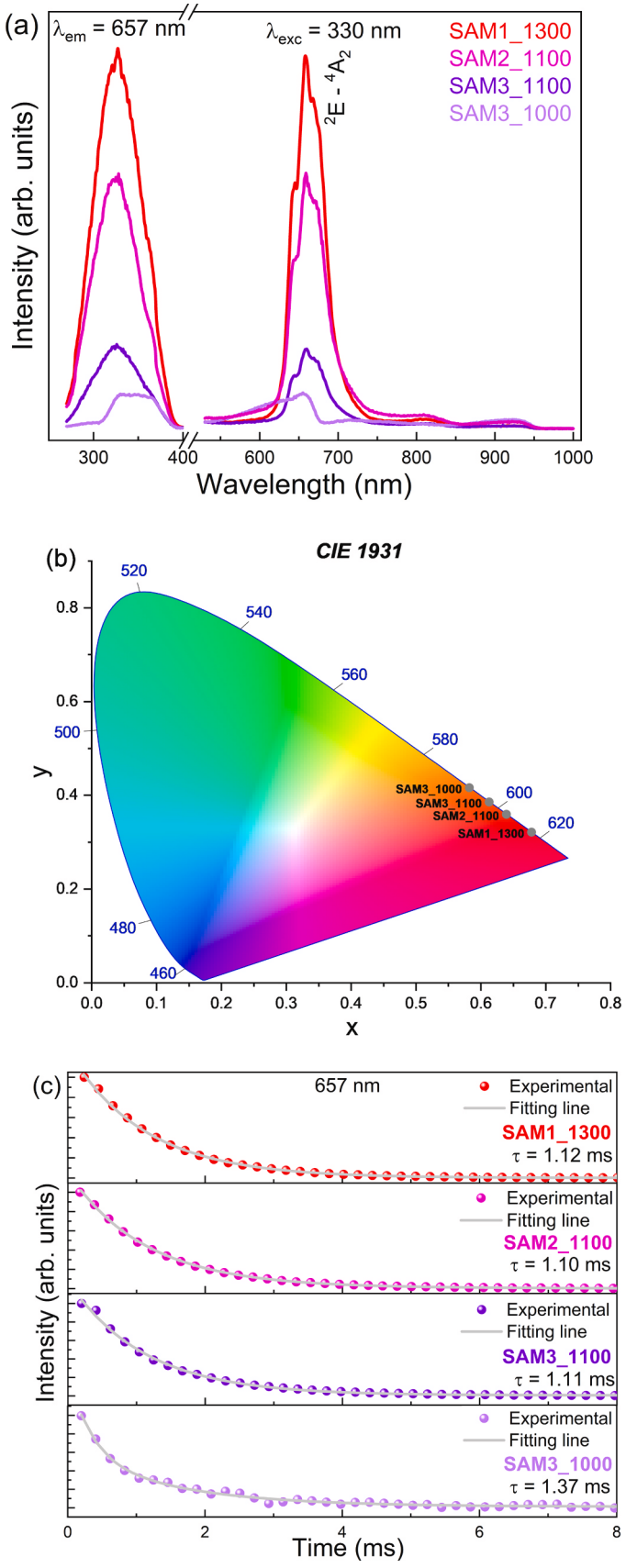

Fig. 5. (a) Excitation and emission photoluminescence spectra, (b) CIE colorimetric coordinates and (c) decay curves of emissions centered at 657 nm for SAM samples.

organic material is constituted by graphene oxide type compound coating a white amorphous powder [36].

Fig. 3 shows XRD patterns for SAM1, SAM2 and SAM3 samples annealed at temperatures between 1000 and 1300 °C with different heating rates. Fig. 3(a) presents XRD for SAM1 sample annealed at 1000, 1100, 1200 and 1300 °C for 2 h with a controlled heating rate of 10 °C/min. As can be seen in this Fig., SAM1 samples annealed at 1000 and 1100 °C exhibit broaden diffraction peaks related to γ-Al2O3 and other rich-strontium crystallographic phases whose crystallites do not present size larger than few nanometers. This statement is in agreement with the observation of an exothermic event at temperature below 1000 °C according to DTA curve shown in Fig. 2(b). Otherwise, SAM1 samples annealed at 1200 and 1300 °C present higher degree of crystallinity and the characteristic diffraction peaks related to the magnetoplumbite phase of $SrAl_{12}O_{19}$ with *P63/mmc* space group. The diffractogram of this structure according to ICSD 114304 database number is also exhibited in Fig. 2(b), indicating that it matches very well with these experimental diffractograms. It is important to highlight the presence of diffraction peaks in minor concentrations of γ-Al2O3 and $SrAl_4O_7$ even in these high-annealing temperature diffractograms.

Fig. 3(b) presents XRD patterns for SAM2 sample annealed at 1000 and 1100 °C with very fast heating rate. Concerning SAM2_1000, the diffractogram in this Fig. also depicts lower degree of crystallinity similar to SAM1 sample, with broaden diffraction peaks related to γ-Al_2O_3 and other rich-strontium crystallographic phases. However, diffractogram for SAM2 sample annealed at 1100 °C presents the XRD reflections associated to the hexagonal phase of $SrAl_{12}O_{19}$ with lower concentration of γ-Al_2O_3 phase. As aforementioned in experimental procedure section, in Route 2 the dried resin is thermally treated under N_2 flux in two steps: at 250 °C for 30 min with heating rate of 1 °C/min and at 400 °C for 24 h with heating rate of 10 °C/min. The first step with slow heating rate is essential to avoid non-uniform polymeric degradation, which can induce hot spots due to localized strong combustions. As a consequence, heterogeneities in the dried powder can occur [30]. These chemical inhomogeneities favor the formation of intermediary phases, such as γ-Al_2O_3 in lower temperatures. Thus, this procedure enables the formation of the magnetoplumbite phase at a lower temperature than the Route 1.

XRD patterns for SAM3 samples are presented in Fig. 3(c). The diffractogram for sample annealed at 1000 °C also exhibits broaden peaks of γ-Al_2O_3 and other rich-strontium phases with lower degree of crystallinity. Nevertheless, as the time of the annealing is increased to 4 h, it is observed the formation of the magnetoplumbite structure. As a result, the temperature for the formation of $SrAl_{12}O_{19}$ is reduced by 300 °C compared to, for example, the conventional synthesis through the polymeric precursor method. This reduction is due to (i) the prevention of the formation of the hot spots with the procedure at lower temperatures of thermal treatments like Route 2 but also due to (ii) remanent organic precursors after annealing at 700 °C under N_2 atmosphere, ball milling and very fast heating. This process during the crystallization stage reduces the heat and mass diffusion length for ions with different mobilities that are dominant in the generation of molecular level inhomogeneities [30]. Furthermore, SAM3_1100 sample does not present secondary phase, only peaks related to $SrAl_{12}O_{19}$ compound in the diffractogram.

Table 1 summarizes synthesis temperature of SAM samples of this present study, as well as the crystallization temperature and the phase purity for several synthesis methods. Semi-quantitative phase analysis through peak intensity ratio was also determined and the values are presented in Table 2. Furthermore, in order to evaluate the crystalline degree of the samples, full width at half-maximum (FWHM) values for (114) peaks in XRD diffractograms were calculated. The values of FWHM are equal to 0.150(5)°, 0.169(4)°, 0.200(4)° and 0.346(5)° for SAM1_1300, SAM2_1100, SAM3_1100 and SAM3_1000 samples, respectively. These results confirm that higher synthesis temperature leads to the higher degree of crystallinity observed for SAM1_1300

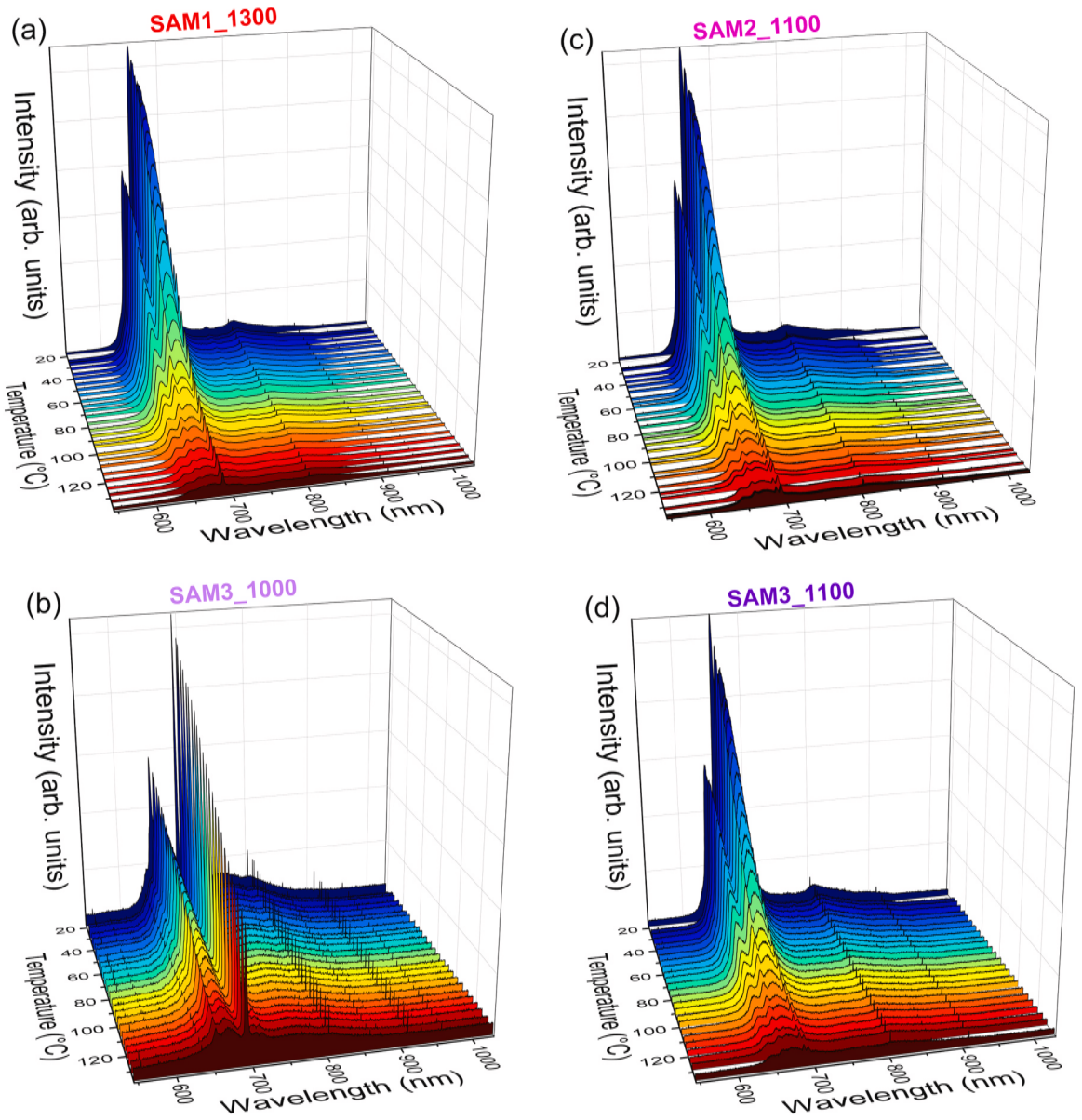

Fig. 6. Photoluminescence spectra as a function of the temperature for (a) SAM1_1300, (b) SAM3_1000, (c) SAM2_1100 and (d) SAM3_1100 samples.

sample. On the other hand, SAM3_1000 sample exhibits the widest diffraction peak and the lowest crystallinity degree.

In order to evaluate the morphology of SAM samples, SEM images were acquired and are shown in Fig. 4. As can be seen in Fig. 4(a) and (b), SAM1_1300 sample exhibits a heterogeneous form consisting of hexagonal-like particles with size of about several hundred nanometers with smaller round particles at nanoscale ranging between 100 and 200 nm. The hexagonal shape is characteristic of SAM samples even prepared through other procedures such as hydrothermal method [21]. The non-uniform behavior in these micrographs is related to the uncontrolled intense combustion of organics with O_2 content during the thermal treatment which can induce hot spots and chemical heterogeneities in Route 1, as discussed previously. On the other hand, Fig. 4(c) and (d) presents more homogeneous morphology for SAM_3_1000 sample comprising particles in submicrometer range with width from 100 to 200 nm and length from 400 to 700 nm.

Fig. 5(a) shows excitation and emission photoluminescent spectra for the SAM samples. In this figure, a broad emission in the excitation spectrum centered at 330 nm when the emission at 657 nm is monitored is observed for all samples. This broad band is associated with the spin-allowed transition by selection rules of the type $^4A_2 \rightarrow {}^4T_1$, typical of Mn^{4+} ions [15,18]. The emission spectra with an excitation wavelength of 330 nm exhibit a multi-peak configuration in the red region centered at 657 nm, which has been attributed to the $^2E \rightarrow {}^4A_2$ type transition and its phonon sidebands [15,18]. In this hexaluminate structure, Mn^{4+} ions occupy the Al^{3+} sites due to their similar ionic radii: 0.0535 and 0.0530 nm, respectively. These Al^{3+} sites can exhibit AlO_4 (one site), AlO_5 (one site), and AlO_6 (three sites) coordination, where the red emission due to the $^2E \rightarrow {}^4A_2$ transition is relatively weak for the tetrahedral sites (AlO_4) compared to the octahedral sites (AlO_6) due to a symmetry breaking of the local crystal lattice [15]. Also in Fig. 5(a), a decrease in the intensity of these emissions is observed for samples prepared through Route 3 compared to Route 2 and Route 1. This decreasing is explained in terms of the lower degree of crystallinity and the existence of secondary phases as discussed in XRD results. This same tendency is also observed in the FWHM values obtained for SAM samples. A higher crystallinity reduces crystal lattice defects, thereby decreasing non-radiative relaxations that cause thermal quenching, increasing emission efficiency and resulting in higher values of relative sensitivity [37,38].

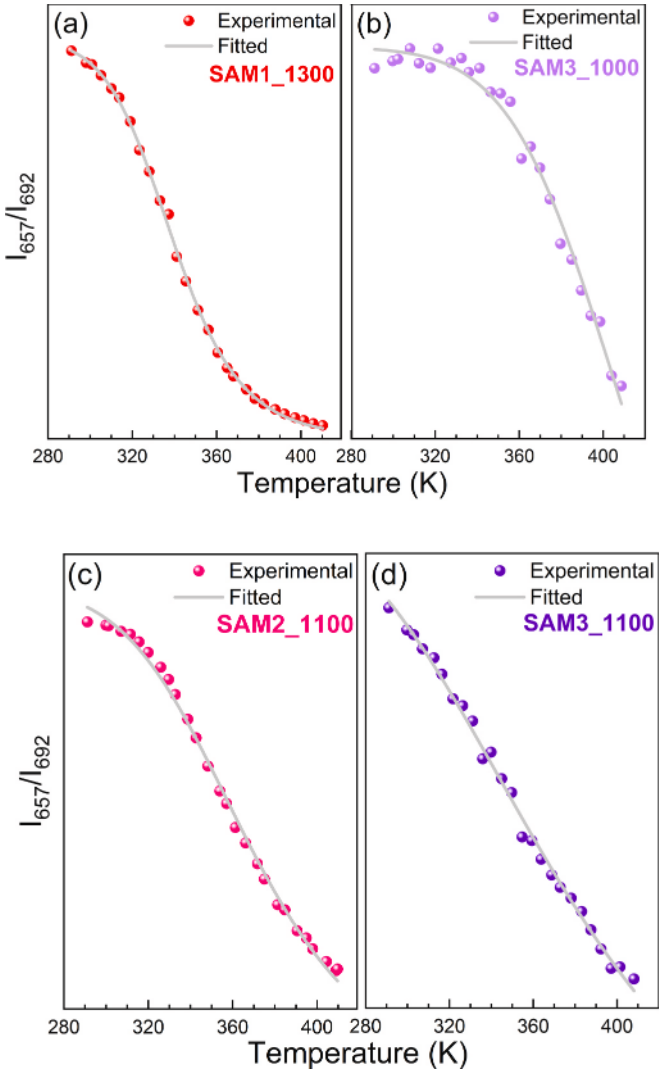

Fig. 7. FIR curves as function of the temperature for (a) SAM1_1300, (b) SAM3_1000, (c) SAM2_1100 and (d) SAM3_1100 samples.

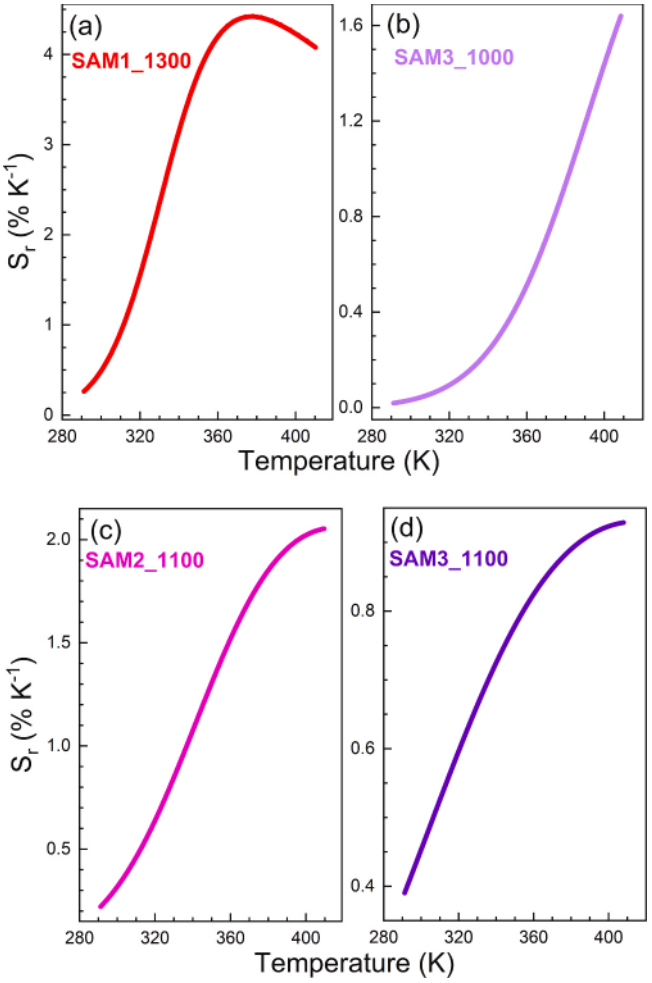

Fig. 8. Relative thermal sensitivity for (a) SAM1_1300, (b) SAM3_1000, (c) SAM2_1100 and (d) SAM3_1100 samples.

Fig. 5(b) exhibits CIE colorimetric coordinates for SAM samples calculated from the emission spectra. The obtained (x, y) values for SAM1_1300 sample are (0.678, 0.321), which are very close to pure red values in the chromaticity diagram (0.67, 0.33), make this sample suitable for technological applications with red emission [5]. As the annealing temperature decreases through Routes 2 and 3, the saturated red CIE coordinates change into the orange area of the chromaticity diagram, also for values in the highly saturated region. This variation is related to the emergence of a broad emission around 629 nm and differences of intensity in the phonon sideband region due to the existence of secondary phases (for instance, $SrAl_4O_7$ compound) and the lower degree of crystallinity.

Luminescence decay curves of the typical Mn^{4+} emission monitored at 657 nm under excitation of 330 nm for SAM samples are shown in Fig. 5(c). All experimental curves follow a second-order exponential decay formula as indicated by the adjusted curves. The fluorescence intensity for lifetime emission can be calculated by the following equation [39]:

$$I(t) = A_1 e^{\frac{-t}{\tau_1}} + A_2 e^{\frac{-t}{\tau_2}}, \quad (1)$$

where $I(t)$ is the intensity at the time t, A_1 and A_2 are the amplitudes constants for each component and τ_1 and τ_2 are the fast and slow exponentials components of the lifetime. The average decay time τ can be calculated according to the expression [39]

$$\tau = \left(A_1\tau_1^2 + A_2\tau_2^2\right)/\left(A_1\tau_1 + A_2\tau_2\right). \quad (2)$$

The fast and slow components for SAM samples are associated with different Al sites that Mn^{4+} occupying at $SrAl_{12}O_{19}$ magnetoplumbite structure [15]. The average lifetime for emission at 657 nm is similar for all samples (~1.11 ms) and in the millisecond range, restricted from the spin-forbidden transitions within its d-shell [39]. This range value is in agreement with the lifetime for Mn^{4+} ions incorporated into host matrix of strontium hexaluminate [19]. Furthermore, the lifetime in this range can be useful for fast response applications of red phosphors. These results indicate similar local structure configuration for all analyzed samples, except for SAM3_1000 sample. The calculated average lifetime for this sample is $\tau_=$ 1.37 ms, which is consistent with the fact that this sample exhibits a small amount of secondary $SrAl_4O_7$ phase, resulting in a different environment around Mn^{4+} ions compared to $SrAl_{12}O_{19}$ host lattice.

Optical thermometry measurements were carried out with an excitation of 405 nm at different temperatures ranging from room temperature to 140 °C. As observed in Fig. 5(a), the broad band between 269 and 385 nm in the excitation spectra is associated with the spin-allowed transition by selection rules of the type $^4A_2 \rightarrow {}^4T_1$, typical of Mn^{4+} ions [15,18]. Another broad band, although with lower intensity, between 385 and 440 nm also relative to $^4A_2 \rightarrow {}^4T_1$ transition is described [15, 18]. Both excitation band, after non-radiative process, result in the $^2E \rightarrow {}^4A_2$ type transition and red emission around 657 nm [15,18]. Thus, the

Table 3
Relative thermal sensitivity S_r for several rare-earth- and/or Mn^{4+}-doped compounds using FIR method.

Phosphor	Temperature range (K)	$S_{r,max}$ (% K^{-1})	Ref.
$SrGdLiTeO_6$:Mn^{4+},Sm^{3+}	298–573	8.69	[53]
YAG:Eu^{3+},Mn^{4+}	303–523	4.81	[54]
$SrAl_{12}O_{19}$:Mn^{4+}[(a)]	291–413	4.41	this work
$BaAl_{12}O_{19}$:Mn^{2+}/$SrAl_{12}O_{19}$:Mn^{4+}	293–406	4.37	[19]
$Ca_2Sb_2O_7$:Eu^{3+},Mn^{4+}	303–393	4.07	[55]
$LaLiTiO_3$:Tm^{3+},Mn^4	298–523	3.49	[39]
Sr_2LuSbO_6:Mn^{4+}	38–578	2.89	[56]
YPO_4:Yb^{3+},Tm^{3+},Ho^{3+}	303–563	2.86	[52]
Ca_2LaSbO_6: Mn^{4+}, Eu^{3+}	273–473	2.6	[57]
La_2MgTiO_6:Dy^{3+},Mn^{4+}	298–480	2.31	[58]
$CaGdAlO_4$: Mn^{4+}, Tb^{3+}	298–523	2.23	[59]
Ba_2ScAlO_5: Yb^{3+},Er^{3+}	298–358	1.78	[60]
$SrAl_{12}O_{19}$:Mn^{4+}[(b)]	291–413	1.63	this work
$SrBaMg_2(PO_4)_2$:Ce^{3+},Eu^{2+},Na^+	298–573	1.57	[61]
$SrGdLiTeO_6$:Mn^{4+},Tb^{3+}	298–573	1.49	[62]
$MgTiO_3$:Mn^{4+}	73–323	1.2	[63]
$Mg_{28}Ge_{7.55}O_{32}F_{15.04}$:$Ga^{3+}$, Mn^{4+}	303–473	0.68	[64]
$Ca_{14}Al_{10}Zn_6O_{35}$:Ti^{4+},Mn^{4+}	303–523	0.57	[65]
$SrAl_{12}O_{19}$:Mn^{4+}	273–393	0.27	[18]
$ZnAl_2O_4$:Cr^{3+},Mn^{2+}	80–100	0.25	[66]

[(a)]SAM1_1300
[(b)] SAM3_1000 samples

characteristic Mn^{4+} red emission can be excited via a wavelength of 405 nm, which can be reached with affordable devices such as diode lasers. They are relatively inexpensive and involve fewer safety issues compared to UV lasers, making them more accessible for various applications, including luminescence thermometry [40]. The emission spectra for Mn^{4+} ions as a function of the temperature is exhibited in Fig. 6 for SAM samples. Similarly to photoluminescence curves at room temperature in Fig. 5(a), the emission spectra is characterized by multi-peak configuration composed by phonon side bands. The intensity of all emission lines decreases gradually as the temperature increases form all SAM samples due to the non-radiative transitions that induce thermal quenching [39]. Moreover, a sharp emission around 692 nm is observed whose intensity varies as a function of the temperature or the preparation route compared to the other regions of the spectra. This emission is attributed to the zero-phonon line (ZPL) for Mn^{4+} ions [41] and presents a different quenching behavior with the temperature. Different quenching rates become available the use of FIR for optical thermometry since ratiometric method is more reliable as aforementioned [10,42]. As the annealing temperature decreases for different routes of preparation, the intensity of the phonon sidebands decreases compared to ZPL intensity. This quenching is ascribed to the lower crystallinity degree shown by the structural characterization of this work. Concerning ZPL, the degree of crystallinity plays a crucial influence on the intensity, width, position, stability and electron density distribution in fluorescence materials [43]. ZPLs correspond to purely electronic transitions without phonon involvement, making them extremely narrow and sensitive to the local environment. Specifically, for ZPL of Mn-doped fluorescence oxide materials, the emission energy of Mn^{4+} corresponds to the hybridization, which is related to the Mn–O bond length and O–Mn–O bond angle [44]. A longer Mn–O bond length and larger O–Mn–O bond angle distortion generally lead to a smaller Mn–O hybridization, and then contribute to higher emission energies [44]. Therefore, crystalline defects can be the origin of local distortion, resulting in higher intensities of ZPLs [44–46]. This statement explains the fact that ZPL emission is more pronounced than phonon-side bands (PSB) for SAM3_1000 sample in comparison with the other samples. Conversely, the structural order in crystalline materials enhances the coupling between electronic states and phonon modes, leading to more pronounced PSB emissions [47,48].

Thus, Fig. 7 shows the intensity ratio of emissions around 657 and 692 nm (I_{657}/I_{692}) for all SAM samples as a function of the temperature. As can be seen in this Fig., FIR of the abovementioned emissions shows non-monotonic behavior, with a gradual decrease of FIR values as the temperature increases. The experimental behavior of the intensity of a fluorescence emission with temperature can be expressed according to the Mott-Seitz relation [10]:

$$I(T) = \frac{I_0}{1 + Ae^{\frac{-E_a}{k_B T}}}, \quad (3)$$

where $I(T)$ is the intensity in a given temperature T, I_0 is the initial intensity of the emission, A is a constant, k_B is the Boltzmann constant and E_a is the activation energy. Thus, the intensity ratio can be summarized approximately according to the following expression: $FIR \approx B + Cexp(-\Delta E/k_B T)$ [19]. Fig. 7 shows the fitted curve considering this Mott-Seitz model for all SAM samples and the calculated curves closely match the experimental values. While lanthanide emission typically follows the Boltzmann distribution, the luminescence of Mn^{4+} is governed by intense electron-phonon coupling and thermal quenching [19]. This quenching occurs when rising temperatures activate non-radiative relaxation channels of optically excited electrons. In systems like Mn^{4+}-doped hexaluminates (a $3d^3$ configuration in octahedral symmetry), the radiative rate is inherently temperature-dependent [10]. Although the electronic transitions are dipole-forbidden, they become partially allowed through coupling with asymmetric lattice vibrations that introduce odd-parity crystal field components [19]. The Mott-Seitz model explains this behavior using a configuration coordinate diagram consisting of two shifted parabolas representing the ground and excited state potential energies [10]. As thermal energy increases, an excited electron can reach the intersection point where the two parabolas cross. At this crossing point, electron transition can occur non-radiatively from the excited state back to the ground state. This model is ideal for describing the quenching of broadband and Mn^{4+} ($^2E \rightarrow {}^4A_2$) luminescence emissions, which is highly sensitive to this parabolic crossover [10]. This model is not suitable for narrow line of *f-f* transitions in trivalent lanthanides or transition metal ions where the excited and ground state parabolas show no relative shift [10].

The strong temperature-dependent behavior for SAM samples indicates a promising potential for application which use the method of FIR in the realm of temperature sensing technologies [19,39]. This applicability can be assessed by the thermometric performance, in which the relative thermal sensitivity S_r allows comparison between thermometers irrespective of their type or detection mechanism and can be calculated as follows [19,42]:

$$S_r = 100 \times \left|\frac{1}{FIR}\right|\left|\frac{\partial FIR}{\partial T}\right|. \quad (4)$$

S_r values for SAM samples are depicted in Fig. 8. As can be seen in this Fig., the sensitivity curve increases gradually from the initial temperature and then reached the maximum values, ending up with a monotonically decreasing trend for SAM1_1300 sample. The maximum value of S_r ($S_{r,max}$) for this sample is 4.41%K^{-1} at 375 K, a higher value compared to $SrAl_{12}O_{19}$:Mn prepared by co-precipitation method with same annealing temperature [18]. The S_r values for other three SAM samples also present gradual increase, but without decreasing for higher measured temperatures. Moreover, even the SAM3_1000 sample, which was synthesized with the lowest annealing temperature in this work presents maximum S_r = 1.63%K^{-1} at 406 K whereas a value of 0.23% K^{-1} at 398 K is reported for this compound at literature also using ratiometric method [18]. Table 3 summarizes several maximum S_r values for phosphors with rare-earth and/or Mn^{+4} ions as activator and FIR method.

In the Fig. 9, FIR values at 657 and 692 nm at room and maximum

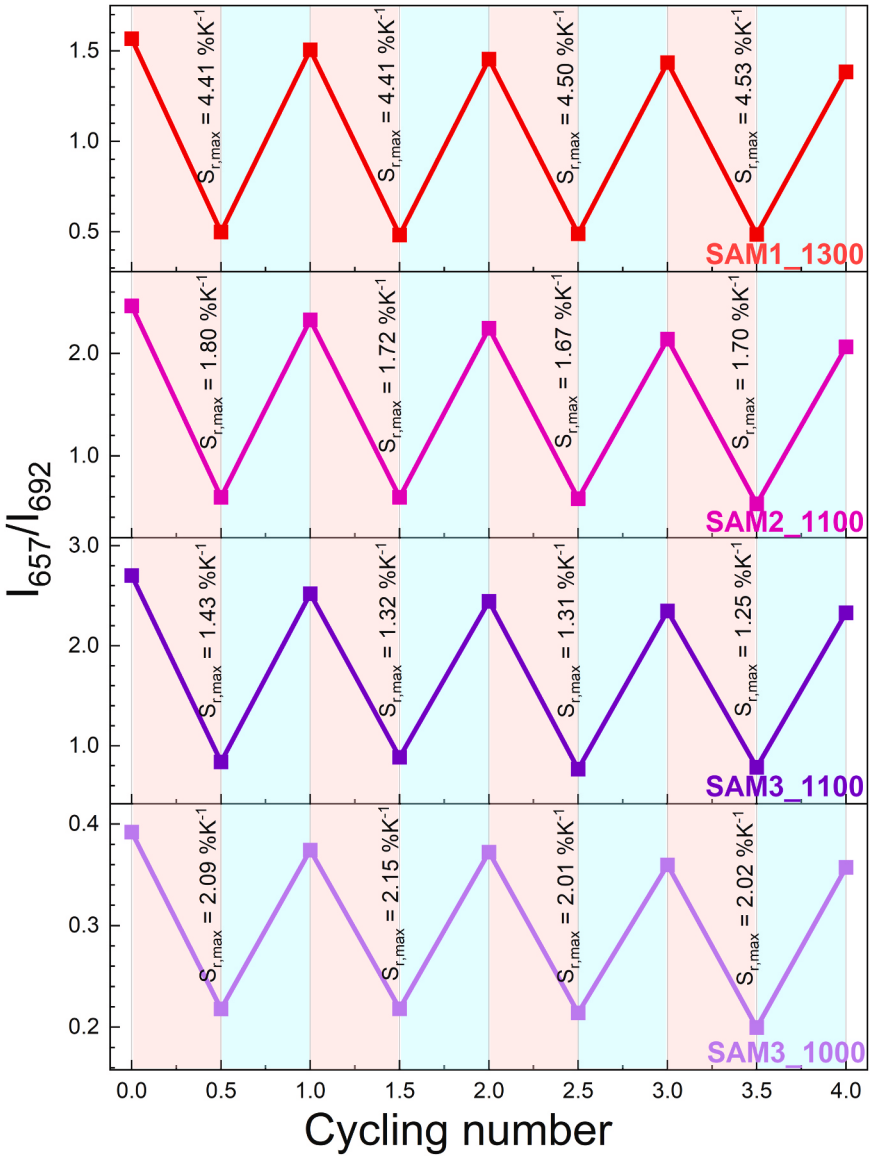

Fig. 9. FIR values at 657 and 692 nm at room and maximum temperatures through four heating-cooling cycles.

temperatures were collected through four heating-cooling cycles. The FIR values were acquired raising from room temperature up to 410 K and cooled naturally. Then, the heating-colling cycles were sequentially repeated and the results prove the samples have good repeatability. Furthermore, in this Fig., $S_{r,max}$ values calculated from FIR during heating for each cycle are also presented, which results reveal reproducibility through several cycles. Consequently, these values also demonstrate FIR calibration reproducible across repeated measurements.

Concerning secondary phases in SAM samples, it is noteworthy the presence of multiple aluminum coordination environments (AlO_6, AlO_5, AlO_4) in $SrAl_{12}O_{19}$ structure [15]. $SrAl_4O_7$ structure, in contrast, can be represented as a framework of edge-shared SrO_7 polyhedra which are connected with only two types of apex-shared AlO_4 tetrahedra [49]. The coordination geometry — whether octahedral (AlO_6), pentahedral (AlO_5), or tetrahedral (AlO_4) — directly influences the crystal field splitting, nonradiative losses, and thus the emission characteristics [15,50,51]. Octahedral sites are highly symmetric, provide a strong crystal field and is energetically favored for Mn^{4+} ions substitution due to size and charge compatibility. Concerning pentahedral sites, they present intermediate symmetry, being less favorable for Mn^{4+} ions. Finally, tetrahedral sites are least symmetric, generally not preferred by Mn^{4+} ions due to suboptimal crystal field stabilization. Thus, the red emission due to the $^2E \rightarrow {}^4A_2$ transition is relatively weak for the tetrahedral sites compared to the octahedral sites due to a symmetry breaking of the local crystal lattice, weaker crystal field, increased nonradiative losses and less defined ^2E state (inefficient red emission). [15,51]. Furthermore, existing literature is limited to a single publication reporting typical Mn^{4+} fluorescence of Mn-doped $SrAl_4O_7$ [49], although Mn atoms occupying AlO_6 octahedra cannot be discarded due the observed $SrAl_2O_4$ secondary phase observed in the samples of this study. Based on these facts and small amount of $SrAl_4O_7$ phase in some $SrAl_{12}O_{19}$:Mn samples, Mn^{4+} emission from Al sites of the secondary phase do not materially contribute to the observed FIR behavior.

The comparison of maximum S_r for SAM samples with several phosphors reveals that the studied samples of this work show values comparable to higher sensitivity of FIR thermometers. Furthermore, these values are similar to the highest values found for phosphors doped or co-doped with rare-earths and, in general, considerably higher when compared with phosphors doped with Mn or other transition metals. These results make SAM samples very promising for FIR thermometer applications, including in the first biological window [52].

4. Conclusions

In summary, $SrMn_{0.005}Al_{11.995}O_{19}$ phosphors were successfully synthesized using a modified polymeric precursor method. Combining annealing under N_2 atmosphere and applying very fast heating rate, crystallization temperature of the pure magnetoplumbite phase was successfully lowered by approximately 300 °C, stabilizing the single-phase magnetoplumbite structure at 1000 °C, a temperature notably lower than that required by solid-state reactions or conventional sol-gel methods. This reduction in synthesis temperature is attributed to the suppression of uncontrolled organic combustion and "hot spots", facilitating a more homogeneous reaction at the molecular level. Optical characterization indicates that Mn^{4+} ions effectively substituted Al^{3+} sites in the host lattice, resulting in strong red emission centered at 657 nm with high color purity. The temperature-dependent luminescence properties demonstrated that application of the Fluorescence Intensity Ratio (FIR) technique using the emissions at 657 and 692 nm showed excellent relative sensitivity ($S_{r\text{-}max} = 4.41\%K^{-1}$). These findings validate that the proposed soft chemical synthesis route is an efficient strategy for producing high-quality aluminates and that the resulting $SrAl_{12}O_{19}:Mn^{4+}$ phosphor is a competitive alternative to rare-earth-based sensors for optical thermometry applications.

CRediT authorship contribution statement

Maria Inês Basso Bernardi: Methodology, Investigation, Conceptualization. **Otuka Adriano José Galvani:** Writing – review & editing, Methodology, Investigation, Conceptualization. **Fabio Simões de Vicente:** Writing – review & editing, Project administration, Methodology, Investigation, Funding acquisition, Formal analysis, Conceptualization. **Alexandre Mesquita:** Writing – review & editing, Supervision, Project administration, Methodology, Investigation, Funding acquisition, Formal analysis, Conceptualization. **Thiago Ardana Chaim:** Writing – original draft, Methodology, Investigation, Conceptualization.

Declaration of Competing Interest

The authors declare the following financial interests/personal relationships which may be considered as potential competing interests: Alexandre Mesquita reports financial support was provided by State of Sao Paulo Research Foundation (FAPESP), National Council for Scientific and Technological Development (CNPq) and Coordenação de Aperfeiçoamento de Pessoal de Nível Superior - Brasil (CAPES).

Acknowledgments

This research used resources of The São Paulo Research Foundation – FAPESP (through projects 2024/22584–9 and 2013/12993–4), National Council for Scientific and Technological Development – CNPq (through projects 130660/2025–6, 432977/2018–0, 427220–2018–1 and 302743/2014–6). This study was financed in part by the Coordenação de Aperfeiçoamento de Pessoal de Nível Superior - Brasil (CAPES) - Finance Code 001. The authors express their gratitude to Daniel Angeli de Moraes for technical support

Appendix A. Supporting information

Supplementary data associated with this article can be found in the online version at doi:10.1016/j.jallcom.2026.187207.

References

[1] R.S. Ukare, V.B. Pawade, S.J. Dhoble, 1 - Brief history and scope of phosphor, in: V. B. Pawade, R.L. Kohale, S.J. Dhoble, H.C. Swart (Eds.), Phosphor Handb. Woodhead Publ. (2023) 3–32, https://doi.org/10.1016/B978-0-323-90539-8.00001-2.

[2] L. Zheng, J. Kuang, J. Shen, H. Wu, H. Wu, Y. Luo, G.-H. Pan, Z. Hao, L. Zhang, J. Zhang, Spectral broadening in Cr3+-doped Sr0.92Mg0.91Al10.1O17 NIR phosphor realized by multi-crystallographic site occupation, ACS Appl. Opt. Mater. 1 (2023) 1150–1155, https://doi.org/10.1021/acsaom.3c00086.

[3] L. Wang, S. Xiao, X. Yang, Long-Wavelength Broadband Near-Infrared ZrTe3O8: Cr3+, Ti4+ Phosphor of High Luminescence Quantum Yield and Excellent Thermal Stability, ACS Appl. Opt. Mater. 3 (2025) 248–258, https://doi.org/10.1021/acsaom.4c00350.

[4] B. Santra, S. Pal, A. Kanjilal, Tuning Visible-to-Near Infrared Dual-Band Emission in ZnO@β-SiC Composite Phosphor, ACS Appl. Opt. Mater. 2 (2024) 687–696, https://doi.org/10.1021/acsaom.4c00087.

[5] G.K. Ribeiro, T.A. Chaim, M.I. Basso Bernardi, A.C. Roveda, A.J. Galvani Otuka, F. S. de Vicente, A. Mesquita, Unraveling the effect of Al-doping on the local structure and the photoluminescence of CaTiO3:Pr nanophosphor, Materials Science Engineering B 316 (2025) 118125, https://doi.org/10.1016/j.mseb.2025.118125.

[6] T. Chen, H. Zeng, Y. Guo, X. Wu, Ultraviolet-triggered red-emitting NaEuF4:Tb3+ nanorods for white LED, ACS Appl. Nano Mater. 8 (2025) 1428–1435, https://doi.org/10.1021/acsanm.4c05855.

[7] X. Liang, L. Fang, X. Li, X. Zhang, F. Wang, Activatable near infrared dye conjugated hyaluronic acid based nanoparticles as a targeted theranostic agent for enhanced fluorescence/CT/photoacoustic imaging guided photothermal therapy, Biomaterials 132 (2017) 72–84, https://doi.org/10.1016/j.biomaterials.2017.04.006.

[8] M.H. Abbas, H. Ibrahim, A. Hashim, A. Hadi, Ameliorating and tailoring the features of silica-silicon carbide nanoceramic doped polyethylene oxide for promising optoelectronics applications, Silicon 17 (2025) 697–707, https://doi.org/10.1007/s12633-025-03227-5.

[9] A. Hashim, H. Ibrahim, F.L. Rashid, A. Hadi, Synthesis and augmented morphological and optical properties of Si3N4-TiN inorganic nanostructures doped PVP for promising optoelectronics applications, J. Inorg. Organomet. Polym. Mater. 35 (2025) 827–837, https://doi.org/10.1007/s10904-024-03324-9.

[10] L. Marciniak, K. Kniec, K. Elżbieciak-Piecka, K. Trejgis, J. Stefanska, M. Dramićanin, Luminescence thermometry with transition metal ions. A review, Coord. Chem. Rev. 469 (2022) 214671, https://doi.org/10.1016/j.ccr.2022.214671.

[11] Z. Chen, L. Wang, G. Huang, J. Xiong, Y. Jiang, B. Qu, Temperature-dependent luminescence of KCl:Sb3+ and its thermometry applications, ACS Appl. Opt. Mater. 3 (2025) 463–470, https://doi.org/10.1021/acsaom.4c00530.

[12] H.C. Vasconcelos, Fundamental Concerns of Optical Fluorescence Intensity Ratio-Based Thermometry, in: A.M. Maghraby (Ed.), Luminescence - Basic Concepts And Emerging New Applications. IntechOpen, London, 2024, https://doi.org/10.5772/intechopen.1005917.

[13] M. Runowski, P. Woźny, N. Stopikowska, I.R. Martín, V. Lavín, S. Lis, Luminescent Nanothermometer Operating at Very High Temperature—Sensing up to 1000 K with Upconverting Nanoparticles (Yb3+/Tm3+), ACS Appl. Mater. Interfaces 12 (2020) 43933–43941, https://doi.org/10.1021/acsami.0c13011.

[14] Y. Wu, Y. Zhuang, R.-J. Xie, K. Ruan, X. Ouyang, Novel Mn4+ doped red phosphors composed of MgAl2O4 and CaAl12O19 phases for light-emitting diodes, Dalton Trans. 49 (2020) 3606–3614, https://doi.org/10.1039/D0DT00118J.

[15] L. Wang, Y. Xu, D. Wang, R. Zhou, N. Ding, M. Shi, Y. Chen, Y. Jiang, Y. Wang, Deep red phosphors SrAl12O19:Mn4+,M (M=Li+,Na+,K+,Mg2+) for high colour rendering white LEDs, Phys. Status Solidi A 210 (2013) 1433–1437, https://doi.org/10.1002/pssa.201228815.

[16] N.T.K. Chi, N.T. Tuan, N.T.K. Lien, D.H. Nguyen, Red Emission of SrAl2O4:Mn4+ phosphor for warm white light-emitting diodes, J. Electron. Mater. 47 (2018) 4571–4578, https://doi.org/10.1007/s11664-018-6320-8.

[17] Z. Liu, K. Qiu, Q. Tang, Y. Wu, J. Wang, Synthesis of Ag+/CaTiO3:Pr3+ with luminescence and antibacterial properties, Adv. Powder Technol. 30 (2019) 23–29, https://doi.org/10.1016/j.apt.2018.10.003.

[18] S.-H. Yang, Y.-C. Lee, Y.-C. Hung, Thermometry of red nanoflaked SrAl12O19:Mn4+ synthesized with boric acid flux, Ceram. Int. 44 (2018) 11665–11673, https://doi.org/10.1016/j.ceramint.2018.03.242.

[19] Y. Zhu, C. Li, D. Deng, B. Chen, H. Yu, H. Li, L. Wang, C. Shen, X. Jing, S. Xu, A high-sensitivity dual-mode optical thermometry based on one-step synthesis of Mn2+:BaAl12O19–Mn4+:SrAl12O19 solid solution phosphors, J. Alloy. Compd. 853 (2021) 157262, https://doi.org/10.1016/j.jallcom.2020.157262.

[20] J.J. Torrez-Herrera, S.A. Korili, A. Gil, Progress in the synthesis and applications of hexaaluminate-based catalysts, Catal. Rev. 64 (2022) 592–630, https://doi.org/10.1080/01614940.2020.1831756.

[21] J. Afshani, A. Perez Mellor, T. Bürgi, H. Hagemann, Crystallization of SrAl12O19 Nanocrystals from Amorphous Submicrometer Particles, J. Phys. Chem. C. 126 (2022) 19336–19345, https://doi.org/10.1021/acs.jpcc.2c04284.

[22] M. Tian, X.D. Wang, T. Zhang, Hexaaluminates: a review of the structure, synthesis and catalytic performance, Catal. Sci. Technol. 6 (2016) 1984–2004, https://doi.org/10.1039/C5CY02077H.

[23] Y. Xu, W. Peng, S. Wang, X. Xiang, P. Lu, Synthesis of SrAl12O19 via citric acid precursor, Materials Science Engineering B 123 (2005) 139–142, https://doi.org/10.1016/j.mseb.2005.07.019.

[24] V. Petrykin, M. Kakihana, Chemistry and Applications of Polymeric Gel Precursors, in: L. Klein, M. Aparicio, A. Jitianu (Eds.), Handbook of Sol-Gel Science and Technology: Processing, Characterization and Applications, Springer International Publishing, Cham, 2018, pp. 81–112, https://doi.org/10.1007/978-3-319-32101-1_4.

[25] J. Li, Q.-H. Yang, H.-H. Li, C.-F. Yang, D.J.-Y. Feng, Developments of crystal structures and photoluminescence properties of Sr 0. 8 5 Eu 0. 1 5 Al 1 2 O 1 9

green phosphors using different synthesis parameters, Mod. Phys. Lett. B 36 (2022), https://doi.org/10.1142/S0217984921410190.
[26] K. Mori, H. Onoda, T. Toyama, N. Osaka, Y. Kojima, Synthesis and fluorescence studies of Eu3+-doped SrAl12O19 phosphor, Opt. (Stuttg.) 180 (2019) 183–188, https://doi.org/10.1016/j.ijleo.2018.11.047.
[27] M.V. Bukhtiyarova, A.S. Ivanova, G.S. Litvak, L.M. Plyasova, Phase composition and texture of Sr(La)Mn hexaaluminates, Kinet. Catal. 50 (2009) 824–829, https://doi.org/10.1134/S0023158409060056.
[28] M.V. Bukhtiyarova, A.S. Ivanova, L.M. Plyasova, G.S. Litvak, A.A. Budneva, E. A. Paukshtis, Structure and acid-base properties of hexaaluminates, React. Kinet. Catal. Lett. 93 (2008) 375–387, https://doi.org/10.1007/s11144-008-5300-z.
[29] K. Dev, A. Selot, G.B. Nair, C.M. Mehare, F.Z. Haque, M. Aynyas, S.J. Dhoble, Synthesis and photoluminescence study of Dy3+ activated SrAl12O19 phosphor, Optik 194 (2019) 163051, https://doi.org/10.1016/j.ijleo.2019.163051.
[30] J.F. Carvalho, F.S. De Vicente, S. Pairis, P. Odier, A.C. Hernandes, A. Ibanez, Synthesis of YAP nanopowder by a soft chemistry route, J. Eur. Ceram. Soc. 29 (2009) 2511–2515, https://doi.org/10.1016/j.jeurceramsoc.2009.03.005.
[31] G. Gasparotto, L.S. Tavares, T.C. Silva, L.J.Q. Maia, J.F. Carvalho, Structural and spectroscopic properties of Eu3+ doped Y4Al2O9 compounds through a soft chemical process, J. Lumin 204 (2018) 513–519, https://doi.org/10.1016/j.jlumin.2018.08.055.
[32] A. Mesquita, M.I.B. Bernardi, L.J.Q. Maia, V.R. Mastelaro, Synthesis and characterization of Pb1-xLaxTiO3 nanocrystalline powders, J. Therm. Anal. Calor. 87 (2007) 747–751, https://doi.org/10.1007/s10973-006-7760-6.
[33] R.C. de Oliveira, D.E. Martins, M.I.B. Bernardi, A. Mesquita, Zn1-xMgxO nanoparticles prepared by the polymeric precursor method: correlation between photoluminescence and local structure, Opt. Mater. 86 (2018) 71–78, https://doi.org/10.1016/j.optmat.2018.09.044.
[34] C.K. Lin, C.M. Zhang, J. Lin, Phase transformation and photoluminescence properties of nanocrystalline ZrO2 powders prepared via the Pechini-type sol-gel process, J. Phys. Chem. C. 111 (2007) 3300–3307, https://doi.org/10.1021/jp0666151.
[35] I. Lazău, C. Păcurariu, R. Băbuţă, The thermal behavior of some polymeric precursors used in CaAl12O19 synthesis, J. Therm. Anal. Calor. 110 (2012) 497–502, https://doi.org/10.1007/s10973-012-2414-3.
[36] Y.Q. Dong, J.W. Shao, C.Q. Chen, H. Li, R.X. Wang, Y.W. Chi, X.M. Lin, G.N. Chen, Blue luminescent graphene quantum dots and graphene oxide prepared by tuning the carbonization degree of citric acid, Carbon N. Y 50 (2012) 4738–4743, https://doi.org/10.1016/j.carbon.2012.06.002.
[37] J. Yuan, Z. Zhang, X. Wang, Y. Cheng, Effects of crystallinity of raw material Y2O3 on luminescent character of Y2O2S:Eu3, Guangxue Xuebao/Acta Opt. Sin. 25 (2005) 1243–1248. ⟨https://www.scopus.com/inward/record.uri?eid=2-s2.0-27544437163&partnerID=40&md5=781525b70e486beb08d2e914870ceeee⟩.
[38] M. Deng, X. Cao, Y. Tang, Z. Zhou, L. Liu, X. Liu, P. Zhang, L.-Y. Chang, H. Ruan, X. Guo, J. Wang, Q. Liu, Gradient defects mediate negative thermal quenching in phosphors, Adv. Photonics 5 (2023), https://doi.org/10.1117/1.AP.5.2.026001.
[39] N. Fu, N. Liu, T. Yin, H. Jin, Z. Liu, D. Wang, L. Guan, F. Wang, X. Li, Photoluminescence properties and Mn4+ → Tm3+ energy transfer of La0.557Li0.33TiO3: Mn4+, Tm3+ for thermometry and NIR-LED applications, J. Alloy. Compd. 1007 (2024) 176463, https://doi.org/10.1016/j.jallcom.2024.176463.
[40] A. Hashemi, A. Vetter, G. Jovicic, M. Batentschuk, C.J. Brabec, Temperature measurements using YAG: Dy and YAG: Sm under diode laser excitation (405 nm), Meas. Sci. Technol. 26 (2015) 075202, https://doi.org/10.1088/0957-0233/26/7/075202.
[41] Y. Ding, N. Guo, X. Lü, H. Zhou, L. Wang, R. Ouyang, Y. Miao, B. Shao, None-rare-earth activated Ca14Al10Zn6O35:Bi3+,Mn4+ phosphor involving dual luminescent centers for temperature sensing, J. Am. Ceram. Soc. 102 (2019) 7436–7447, https://doi.org/10.1111/jace.16660.
[42] I.E. Kolesnikov, D.V. Mamonova, M.A. Kurochkin, V.A. Medvedev, E. Yu Kolesnikov, Multimode optical thermometry using CaWO4 emission band, J. Alloy. Compd. 1007 (2024) 176466, https://doi.org/10.1016/j.jallcom.2024.176466.
[43] A.P. Voitovich, V.S. Kalinov, A.V. Mudryi, V.N. Pavlovskii, L.P. Runets, I. E. Svitsiankou, Zero-phonon lines and electron-phonon interaction characteristics of near-surface layer radiation color centers in lithium fluoride, J. Lumin 172 (2016) 147–153, https://doi.org/10.1016/j.jlumin.2015.11.032.
[44] S. Li, C. Zhang, Q. Zhu, J.-G. Li, Cationic pair substitution in LaAlO3:Mn4+ for octahedral-tilting-dependent zero-phonon line, Inorg. Chem. Front 10 (2023) 638–650, https://doi.org/10.1039/D2QI01683D.
[45] W. Zhang, L. He, Z. Wang, H. Ji, Mn4+-doped Red-emitting Fluoride Phosphors with Intense Zero Phonon Line, Faguang Xuebao/, Chin. J. Lumin. 44 (2023) 1733–1750, https://doi.org/10.37188/CJL.20230107.
[46] Y. Jin, M.-H. Fang, M. Grinberg, S. Mahlik, T. Lesniewski, M.G. Brik, G.-Y. Luo, J. G. Lin, R.-S. Liu, Narrow red emission band fluoride phosphor KNaSiF6:Mn4+ for warm white light-emitting diodes, ACS Appl. Mater. Interfaces 8 (2016) 11194–11203, https://doi.org/10.1021/acsami.6b01905.
[47] A. Chernikov, T. Feldtmann, S. Chatterjee, M. Koch, M. Kira, S.W. Koch, Time-resolved phonon-sideband spectroscopy, Solid State Commun. 150 (2010) 1733–1736, https://doi.org/10.1016/j.ssc.2010.07.034.
[48] D. Wigger, R. Schmidt, O. Del Pozo-Zamudio, J.A. Preuß, P. Tonndorf, R. Schneider, P. Steeger, J. Kern, Y. Khodaei, J. Sperling, S.M. De Vasconcellos, R. Bratschitsch, T. Kuhn, Phonon-assisted emission and absorption of individual color centers in hexagonal boron nitride, 2d Mater. 6 (2019), https://doi.org/10.1088/2053-1583/ab1188.
[49] V. Stadnik, V. Hreb, A. Luchechko, Y. Zhydachevskyy, A. Suchocki, L. Vasylechko, Sol-gel combustion synthesis, crystal structure and luminescence of Cr3+ and Mn4+ ions in nanocrystalline SrAl4O7, Inorg. (Basel) 9 (2021), https://doi.org/10.3390/inorganics9120089.
[50] M. Sagayama, U. Zafari, M. Subhoni, A.M. Srivastava, W.W. Beers, W.E. Cohen, M. G. Brik, T. Yamamoto, Theoretical and experimental investigations of Mn4+ site occupation in CaAl12O19, ECS J. Solid State Sci. Technol. 10 (2021), https://doi.org/10.1149/2162-8777/ac13df.
[51] M. Gao, Y. Pan, Y. Jin, J. Lin, A review on the structural dependent optical properties and energy transfer of Mn4+and multiple ion-codoped complex oxide phosphors, RSC Adv. 11 (2020) 760–779, https://doi.org/10.1039/d0ra08550b.
[52] M. Ding, M. Zhang, C. Lu, Yb3+/Tm3+/Ho3+ tri-doped YPO4 submicroplates: a promising optical thermometer operating in the first biological window, Mater. Lett. 209 (2017) 52–55, https://doi.org/10.1016/j.matlet.2017.07.113.
[53] Z. Wu, L. Li, Y. Wang, F. Ling, Z. Cao, S. Jiang, G. Xiang, X. Zhou, Y. Hua, J.S. Yu, High-sensitivity luminescent thermometer based on Mn4+/Sm3+ dual-emission centers in double-perovskite tellurate, Ceram. Int. 48 (2022) 27664–27671, https://doi.org/10.1016/j.ceramint.2022.06.064.
[54] D. Chen, S. Liu, Y. Zhou, Z. Wan, P. Huang, Z. Ji, Dual-activator luminescence of RE/TM:Y3Al5O12 (RE = Eu3+, Tb3+, Dy3+; TM = Mn4+, Cr3+) phosphors for self-referencing optical thermometry, J. Mater. Chem. C. Mater. 4 (2016) 9044–9051, https://doi.org/10.1039/C6TC02934E.
[55] X. Shi, Y. Chen, G. Li, K. Qiang, Q. Mao, L. Pei, M. Liu, J. Zhong, Designing a dual-wavelength excitation Eu3+/Mn4+ co-doped phosphors for high-sensitivity luminescence thermometry, Ceram. Int. 49 (2023) 20839–20848, https://doi.org/10.1016/j.ceramint.2023.03.217.
[56] H. Li, L. Li, L. Mei, W. Zhao, X. Zhou, Y. Wang, Y. Hua, P. Du, Thermally stable rare-earth-free double perovskite phosphors toward dual-mode optical thermometry and dual-functional lighting sources, J. Mater. Chem. C. Mater. 11 (2023) 12637–12648, https://doi.org/10.1039/D3TC02471G.
[57] H. Fan, Z. Lu, Y. Meng, P. Chen, L. Zhou, J. Zhao, X. He, Optical temperature sensor with superior sensitivity based on Ca2LaSbO6: Mn4+, Eu3+ phosphor, Opt. Laser Technol. 148 (2022) 107804, https://doi.org/10.1016/j.optlastec.2021.107804.
[58] K. Qiang, Y. Ye, Q. Mao, F. Chen, L. Chu, M. Liu, J. Zhong, Dy3+,Mn4+ co-doped phosphors for synergistic luminescent dual-mode thermometer and high-resolution imaging, Mater. Des. 241 (2024) 112906, https://doi.org/10.1016/j.matdes.2024.112906.
[59] Y. Fang, Y. Zhang, Y. Zhang, J. Hu, Achieving high thermal sensitivity from ratiometric CaGdAlO4:Mn4+,Tb3+ thermometers, Dalton Trans. 50 (2021) 13447–13458, https://doi.org/10.1039/D1DT02185K.
[60] J. Hu, X. Bian, R. Wang, L. Liu, N. Ilyas, F. Wang, Z. Song, H. Fu, Giant Enhancement in Upconversion Luminescence of β-Ba2ScAlO5:Yb3+/Er3+ Phosphor by the Intermediate Band through Ca2+ Doping, Chem. Mater. 34 (2022) 3089–3098, https://doi.org/10.1021/acs.chemmater.1c04142.
[61] J. Zhang, D. Yang, G. Chen, Y. Zhang, Emission-tunable Sr1-n-2x-yBanMg2(PO4)2: xCe3+,yEu2+,xNa+ phosphors for optical temperature sensing, J. Alloy. Compd. 725 (2017) 1055–1062, https://doi.org/10.1016/j.jallcom.2017.07.267.
[62] L. Li, X. Li, Z. Wu, Y. Hua, X. Zhou, Y. Wang, Z. Cao, S. Jiang, G. Xiang, J.S. Yu, Designing dual-emission phosphors for temperature warning indication and dual-mode luminescence thermometry, Dalton Trans. 52 (2023) 15798–15806, https://doi.org/10.1039/D3DT01525D.
[63] E. Glais, V. Đorđević, J. Papan, B. Viana, M.D. Dramićanin, MgTiO3:Mn4+ a multi-reading temperature nanoprobe, RSC Adv. 8 (2018) 18341–18346, https://doi.org/10.1039/C8RA02482K.
[64] Z. Yang, Z. Wang, M. Zheng, X. Wang, J. Cui, Y. Yao, L. Cao, M. Zhang, H. Suo, P. Li, Excitation selective thermal characteristics of Mg28Ge7.55−xGaxO32F15.04: Mn4+ and application in single/dual-mode optical thermometry, Mater. Today Commun. 28 (2021) 102660, https://doi.org/10.1016/j.mtcomm.2021.102660.
[65] Y. Ding, N. Guo, M. Zhu, W. Lv, R. Ouyang, B. Shao, Photoluminescence and ratiometric fluorescence temperature sensing abilities of zincate phosphors, J. Lumin 228 (2020) 117600, https://doi.org/10.1016/j.jlumin.2020.117600.
[66] B. Zhu, S. Ren, Y. Liu, D. Zhang, Q. Wang, S. Li, B. Yang, W. Wang, B. Zhang, Influence of Mn2+ ions on the structure, spectral characteristics and optical thermometry performances of ZnAl2O4:Cr3+ multifunctional phosphors, J. Lumin 244 (2022) 118736, https://doi.org/10.1016/j.jlumin.2022.118736.